


Copper-Based Conductive Nanoinks: Scalable Synthesis via Continuous-Flow Microwave-Assisted Polyol Process

Antonio Santana-Otero*, Yilian Fernández-Afonso*, María Salvador, André Van Zomeren, Salvador Bertran-Llorens, María del Puerto Morales* , and Sabino Veintemillas-Verdaguer

Metallic copper nanoparticles are a promising alternative to gold and silver in printed electronics due to their excellent electrical and thermal conductivity. However, their synthesis is often hindered by rapid oxidation and limited scalability. This work presents a microwave-assisted polyol process for the rapid and scalable production of metallic Cu micro- and nanoparticles, performed in air without the need for an inert atmosphere. Ethylene glycol acts as both solvent and reducing agent, while lignin serves as a renewable capping agent. Reaction time is reduced to 10 min in batch mode, and the process is scaled up to a continuous-flow microwave system, achieving production rates of $\sim 5 \text{ g h}^{-1}$. Particle sizes range from 800 to 40 nm depending on lignin content and metal seeding. After pressure or low-temperature (150°C) treatment, the materials reach conductivities between 30 and $100 \mu\Omega\text{-cm}$. These metallic copper nanoparticles show strong potential for use in sustainable conductive inks for flexible and printed electronics.

1. Introduction

Copper nanoparticles (Cu NPs) have emerged as a cost-effective and sustainable alternative to gold and silver nanoparticles for electronics, optics, sensors, catalysts, and medical applications.^[1] With an intrinsically high electrical conductivity comparable to that of silver—the most conductive metal—copper offers excellent electrical performance to be used in printable electronic circuits.^[2,3] In addition, its greater natural abundance and significantly lower cost make it an attractive option for large-scale applications. This combination of high conductivity and

affordability positions Cu NPs as a compelling material for next-generation flexible electronics, which are increasingly central to technologies such as wearable devices and smart environments.^[4,5] However, a major limitation of Cu NPs for these applications is their high susceptibility to oxidation during processing and storage, which can significantly reduce their electrical conductivity even before integration into devices.

The synthesis of Cu NPs presents several challenges, especially when targeting sustainable and scalable production. Traditional methods often rely on strong reducing agents like sodium borohydride (NaBH_4), which effectively reduce Cu^{2+} ions to metallic copper.^[6] However, these reagents produce hazardous by-products, complicating waste management and limiting industrial applicability. Additionally, after the synthesis, it is required to avoid the

formation of copper oxides (Cu_2O , CuO) that degrade the electrical properties of the final product. Despite some advances using eco-friendly reductants, such as plant extracts or ascorbic acid,^[7–9] producing high-purity metallic Cu NPs with minimal oxide contamination at industrial scale remains difficult. One alternative method is the polyol synthesis, where mild reductants like ethylene glycol are used under relatively simple conditions.^[10–12] While this approach reduces the use of hazardous chemicals, it typically involves long reaction times—often up to 24 h—and results in low production efficiencies ($<1 \text{ g h}^{-1}$), making it unsuitable for large-scale manufacturing. To improve scalability, microwave-assisted synthesis has emerged as a promising alternative, offering significantly faster reaction times (minutes) and enhanced energy efficiency.^[13–16] Unlike conventional heating, microwave irradiation provides rapid and uniform volumetric heating, accelerating reaction kinetics and improving nanoparticle yield. However, scaling up microwave-assisted synthesis to large batch reactors remains challenging due to limitations in uniform energy distribution and heat transfer. In this context, the development of continuous-flow reactors with precise control over experimental parameters is essential for the industrial application of microwave-assisted synthesis of metallic nanoparticles in liquid phase. A previous attempt to produce Cu nanoparticles in a microwave flow reactor used tannic acid, yielding mostly highly agglomerated particles (20–60 nm, with $\sim 200 \text{ nm}$ agglomerates) and modest production rates, ranging from 0.3 to 0.6 g h^{-1} .^[17] However, this approach holds considerable potential for improving scalability, as already shown for other nanoparticles such as iron oxide.^[18] Coupling microwave-assisted synthesis in polyol media with

Dr. A. Santana-Otero, Dr. Y. Fernández-Afonso, Dr. M. Salvador, Prof. M. del Puerto Morales, Dr. S. Veintemillas-Verdaguer
Instituto de Ciencia de Materiales de Madrid, ICMM/CSIC, C/Sor Juana Inés de la Cruz 3, 28049, Madrid, Spain

E-mail: antonio.santana@icmm.csic.es

E-mail: y.fafonso@csic.es


E-mail: puerto@icmm.csic.es

Dr. M. Salvador

Department of Physics, University of Oviedo, Campus de Viesques, 33204, Gijón, Spain

Dr. A. Van Zomeren, Dr. S. Bertran-Llorens

The Netherlands Organisation for Applied Scientific Research (TNO), Energy and Materials Transition, Biobased and Circular Technologies Group, P.O. Box 15, 1755 ZG, Petten, The Netherlands

 The ORCID identification number(s) for the author(s) of this article can be found under <https://doi.org/10.1002/eam.2.70164>.

DOI: 10.1002/eam.2.70164

a continuous-flow configuration is expected to improve reaction efficiency, enhance nanoparticle yield and purity, and reduce product variability through better control of temperature, residence time, and mixing conditions.

In the context of conductive inks for printed electronics, the size of nanoparticles needs to be controlled. Particle size directly affects ink stability, deposition quality, and the electrical performance of printed features. For screen printing, which employs high-viscosity inks, larger particles (50–500 nm) can be used without compromising film uniformity. In contrast, inkjet printing requires smaller nanoparticles (1–100 nm) to ensure proper dispersion in low-viscosity formulations and to avoid nozzle clogging. Smaller particles also enhance printing resolution and enable the formation of continuous, conductive films, making them ideal for fine-feature circuit designs.^[19] Therefore, the choice of particle size is not only essential for ensuring compatibility with specific printing techniques but also for improving pattern quality and reducing production costs. As the density of conductive patterns influences the amount of ink required, optimizing nanoparticle size plays a central role in advancing the efficiency and scalability of printed electronic technologies.^[20] In the polyol process, nanoparticle size can be effectively controlled by adding nucleating agents such as silver, palladium, or platinum, which promote heterogeneous nucleation.^[21] In this way, metal species are reduced by the polyol, leading to tiny particles that act as preferential growth sites for the final particles. By adjusting the amount of nucleating agent, the mean particle size can be finely tuned. Heterogeneous nucleation thus provides a reliable route to achieve controlled particle size distribution. In this work, we will explore the use of metallic nucleating agents to modulate the final size of Cu nanoparticles.

An alternative approach for controlling particle size relies on steric stabilization using organic agents (e.g., PVP, dextran, formic acid, lignin) to control nanoparticle growth and protect the nanoparticles against oxidation.^[22–24] Lignin, which can be sourced from various types of lignocellulosic biomass obtained from agricultural and industrial residues, is an appealing additive that aligns with the principles of green chemistry. Its use reflects a circular economy approach, repurposing industrial waste for Cu NP synthesis. Lignin characteristics are dependent on the extraction method, with the most common types being kraft lignin and organosolv lignin.^[25] While kraft lignin is already being highly produced in the paper industry, the high sulfur content and recalcitrant structure make it more difficult to apply this type of lignin. On the other hand, organosolv processes such as Fabiola allow for a sulfur-free and higher reactive lignin, making it more suitable for applications requiring well-defined surface interactions. Incorporating lignin as a capping agent offers a dual benefit: it chemically stabilizes the nanoparticles while reducing the environmental footprint of the overall process.^[26,27] It should be emphasized that, unlike silver or gold, Cu NPs require specific surface conditions to enable proper sintering into conductive networks. Oxide layers act as insulating barriers that prevent particle bonding, while turbostratic carbon, although protective against oxidation, hinders direct metallic contact. Therefore, achieving high electrical performance requires synthesizing Cu NPs with minimal oxide layers and easily removable coatings to facilitate effective sintering at mild temperatures.

To address all these challenges, this study explores the microwave-assisted synthesis of Cu NPs using a polyol method under both batch and continuous-flow conditions. Sodium hydroxide (NaOH) was employed to establish a basic reaction environment, enabling ethylene glycol to function as both solvent and reducing

agent. Additionally, lignin was incorporated as a capping agent to provide chemical stabilization of the nanoparticles. Reactions were conducted in a microwave reactor, with a reaction time of 20 min per batch or a residence time of 20 min in the continuous-flow setup.^[28] This approach aims to develop an efficient, scalable, and environmentally friendly synthesis route for Cu NPs, eliminating the need for external reducing agents while ensuring the production of high-quality nanoparticles for use in printed electronics.

2. Results and Discussion

2.1. Polyol Process Reduction Mechanism

Metallic copper particles, ranging from 40 to 800 nm with irregular shapes, were synthesized by reducing copper ions from copper chloride via the polyol process and assisted by a microwave reactor that helped in accelerating the reaction, in both batch (Figure 1a) and continuous-flow modes (Figure 1b). The low formation of by-products is attributed to the rapid heating and precise thermal control of the microwave-assisted process, as shown by the temperature and power profiles in Figure 1c,d. In both synthesis modes, the copper salt was reduced through the in-situ formation of ethylene glycolates, generated by mixing NaOH and EG, as previously described.^[29]

The formation of this glycolate (monoanion ethylene glycol) occurs when mixing NaOH in EG at 140 °C. Then, when this basic solution is mixed with the copper salt solution, a color change is observed from an initial green to blue, indicating the formation of a copper glycolate (Figure S1 inset, Supporting Information).^[30] The resulting copper glycolate was precipitated using acetone at a 2:1 ratio (Ac:EG) and characterized by XRD (Figure S1, Supporting Information), showing a crystal structure similar to that reported for copper alkoxides.^[31] It should be emphasized that the reduction of the copper salt by ethylene glycolate occurs without additional reducing agents and under an air atmosphere. The complete process is depicted in Figure 1e. Ethylene glycol first undergoes dehydration, releasing a molecule of water to form ethylene glycolate, which donates electrons to reduce Cu(OH)₂ to its metallic state while oxidizing, typically forming acetaldehyde and diacetyl. This process highlights the electron transfer mechanism crucial for redox reactions and metal nanoparticle synthesis, also described for Nickel and Cobalt.^[11]

2.2. Key Parameters in Cu NP Synthesis: Batch Microwave

The effects of key synthesis parameters, including the NaOH/Cu (w/w) ratio (1.5–10.4) and the lignin/Cu (w/w) ratio (0–9.8), on the nature of the copper nanoparticles as well as their particle, crystal, and hydrodynamic sizes were examined.

FCC metallic copper nanoparticles were obtained in the microwave reactor operating in batch mode, in the absence of lignin, for a NaOH/Cu ratio greater than 2.8 (Figure 2a, Table 1). No other phases, such as copper hydroxides or copper oxides, were detected. In contrast, only copper oxide was formed when the ratio was equal to or less than this value. The addition of lignin (SW) as a surfactant during synthesis lowered the required NaOH/Cu ratio to obtain metallic copper (Figure 2b). In this case, metallic NPs were obtained at NaOH/Cu ratios >1.4. A significant reduction in particle size from 678 to 84 nm was observed when increasing the NaOH/Cu ratio from 2.8 to 4.1

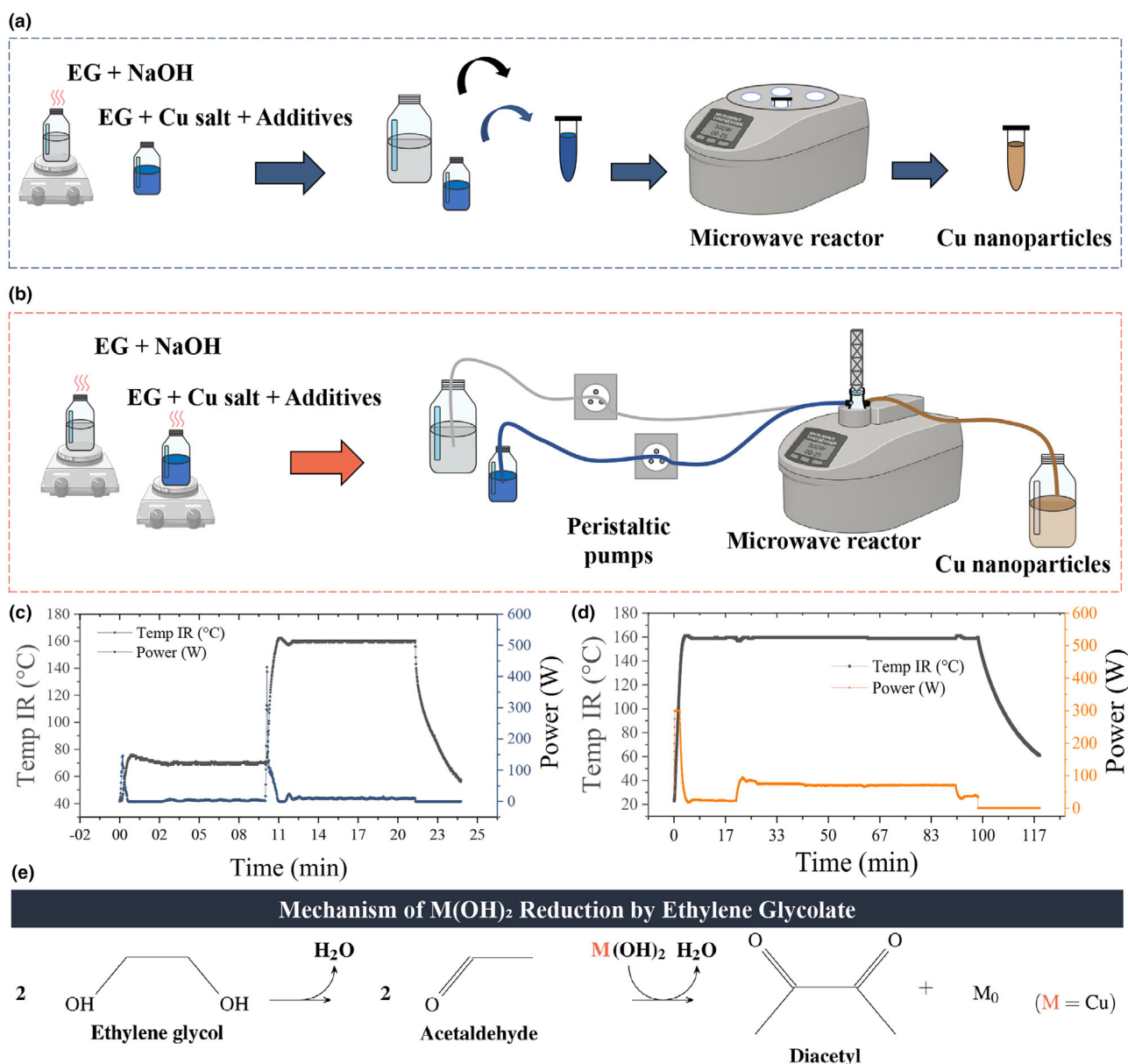


Figure 1. Schematic representation of microwave synthesis processes a) in batch and b) continuous-flow mode. Power and temperature profiles applied during the synthesis processes c) in batch and d) continuous-flow microwave. e) Reduction mechanism of Cu via the oxidation of ethylene glycol.

(Figure 2c,d), accompanied by improved size uniformity, with the standard deviation (σ) decreasing from 86 to 46. However, when the NaOH/Cu ratio exceeded 10, smaller particles tended to agglomerate, resulting in an increase in average particle size ($D_m = 289$ nm) and a broader size distribution ($\sigma = 165$).

Further reduction in particle size to 37 nm can be achieved at high NaOH/Cu ratios (>10) and high lignin content (L/Cu ratio = 9.8), likely due to lignin preventing Cu nanoparticle aggregation. In contrast, increasing the NaOH/Cu ratio from 1.4 to 10.4 in the presence of lignin did not significantly affect particle size (Figure 2c,d). The amount of organic matter on the nanoparticle surface increased from 0 to 6.5 wt% as the L/Cu ratio increased from 0 to 9.8, as evidenced by the TGA analysis in an argon atmosphere (Figure 2e). In the TGA analysis

performed in air, oxidation of the samples became evident above ~ 145 °C, where a mass increase of about 15–25% was observed due to the oxidation of copper particles (Figure 2f). In the presence of lignin, oxidation occurred at a lower temperature due to the combustion of organic matter, which promotes metal oxidation, further enhanced by the nanometer particle size.

Calorimetric studies revealed that increasing the lignin content within the samples raised their glass transition temperature (T_g) (Figure 2g). Notably, the T_g of the sample with low lignin content was below 100 °C, while for the highest lignin content, it is very similar to the T_g of pure lignin (125 °C, Figure 2g), in agreement with previously reported data.^[32] This observation suggests that for the highest lignin content, a significant fraction of lignin is not bound to the

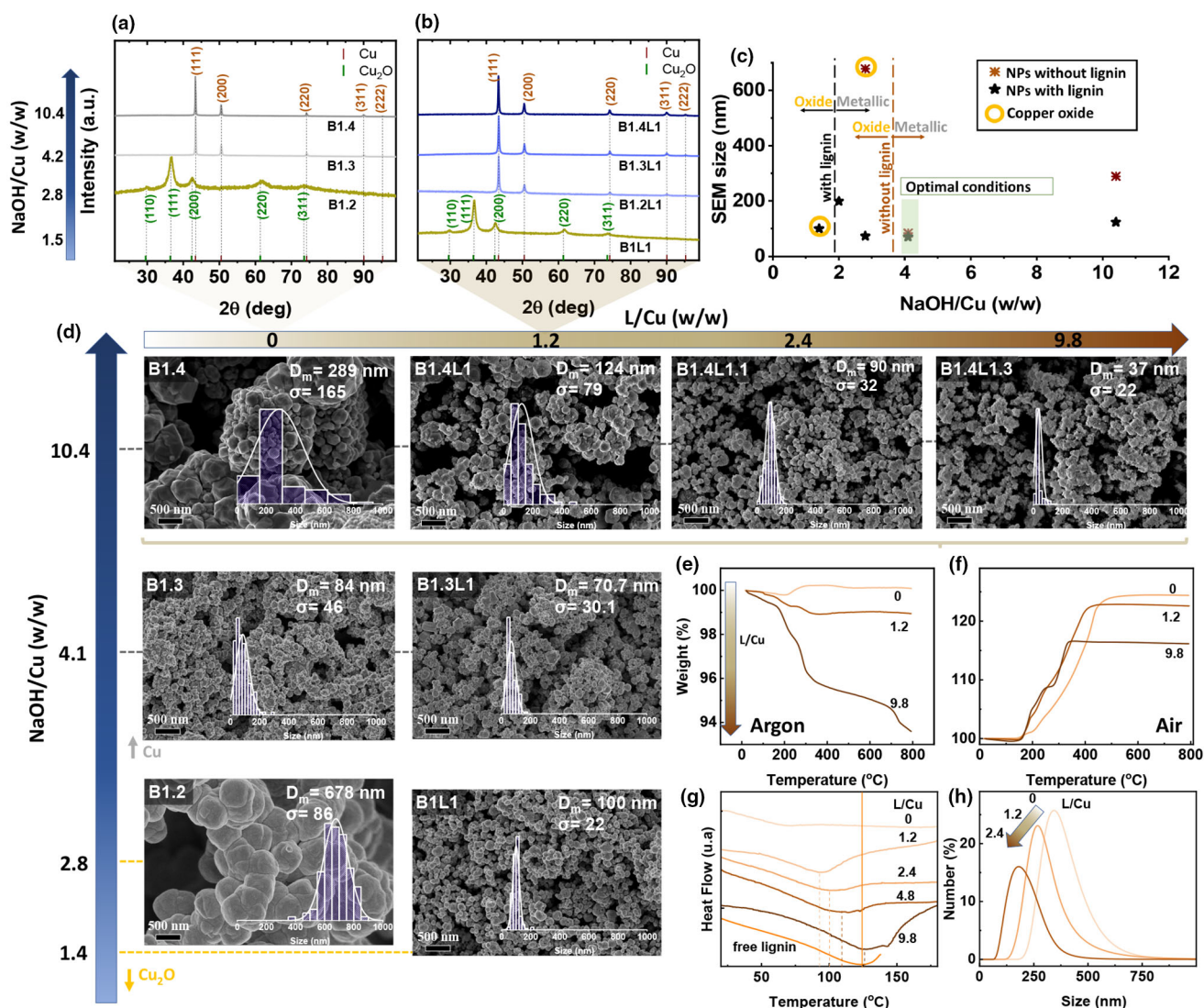


Figure 2. Chemical and structural characterization of Cu NPs synthesized by the microwave-assisted polyol process in batch (B) described in Table 1. a, b) XRD diffractograms at room temperature of Cu NPs at different NaOH/Cu ratio without (left) and with lignin (L = SW) (right); c) Diagram of particle size behavior with increasing NaOH/Cu ratio in synthesis with (L/Cu = 1.2) and without lignin; d) SEM images of Cu NPs under different NaOH/Cu and L/Cu conditions; e, f) Thermogravimetric analysis (in Argon (left)/Air atmosphere (right)); g) Calorimetric measurements by DSC (in Nitrogen atmosphere); and h) Hydrodynamic diameter in EG medium for the Cu NPs synthesized in the presence of different amounts of lignin measured by DLS.

particle surface, and its composition or molecular structure is not significantly altered during the reaction. To investigate potential structural changes that the lignin might undergo during the synthesis, Fourier-transform infrared spectroscopy (FTIR) was carried out for the lignin before and after the heating process in the presence of NaOH and EG (Figure S2, Supporting Information). The resulting FTIR spectra showed no significant differences, indicating that the lignin structure remained largely unaltered throughout the synthesis process. Consequently, for a low amount of lignin, the differences in T_g are due to the binding of lignin to the nanoparticle surface, which is expected to affect the colloidal properties of the nanoparticles in suspension. Thus, as the lignin content increased from 0 to 2.4 L/Cu, a reduction in the hydrodynamic diameter of copper particles in EG was observed

(from 344 ± 29 nm to 254 ± 22 nm and 179 ± 16 nm) (Figure 2h), consistent with the particle size reduction observed by SEM (Figure 2d). However, at higher lignin contents L/Cu > 2.4, the hydrodynamic diameter increased again (from 164 ± 36 nm to 242 ± 22 nm), probably due to the agglomeration or accumulation of the free lignin, as revealed by the calorimetry data. This trend is particularly relevant for the preparation of inks, as the hydrodynamic size directly influences the viscosity, stability, and printability of the ink. A stable suspension with controlled particle size ensures uniform deposition, prevents nozzle clogging, and enhances the overall performance of the ink in printing applications. The XRD size of the Cu NPs was also found to be inversely proportional to the amount of lignin in solution. In conclusion, as the lignin concentration increases, both the particle

Table 1. Summary of reagent concentrations, volumes, and additives (lignin) used in the batch microwave syntheses of Cu nanoparticles under various conditions.

Sample	Batch microwave synthesis						
	Cu salt/Lignin + EG				NaOH+EG		
	Cu salt [M] ^{a)}	L	L/Cu (w/w) ^{b)}	V _{EG} [mL]	NaOH [mmol]	V _{EG} [mL]	NaOH/Cu (w/w) ^{b)}
Cu synthesis							
B1.2	0.5	—	—	5	10	15	2.8
B1.3	0.5	—	—	5	15	15	4.1
B1.4	0.5	—	—	5	37.5	15	10.4
Cu-L synthesis							
B1L1	0.5	SW	1.2	5	5	15	1.4
B1.1L1	0.5	SW	1.2	5	7.5	15	2.1
B1.2L1	0.5	SW	1.2	5	10	15	2.8
B1.3L1	0.5	SW	1.2	5	15	15	4.1
B1.4L1	0.5	SW	1.2	5	37.5	15	10.4
B1.4L1.1	0.5	SW	2.4	5	37.5	15	10.4
B1.4L1.2	0.5	SW	4.9	5	37.5	15	10.4
B1.4L1.3	0.5	SW	9.8	5	37.5	15	10.4
Higher yield Cu-L synthesis							
B2L1	1.8	SW	0.3	5	37.5	15	2.6
B2L2	1.8	WS	0.3	5	37.5	15	2.6
B2L3	1.8	BW	0.3	5	37.5	15	2.6
B2L4	1.8	BW-1DP	0.3	5	37.5	15	2.6

L, Lignin; V_{EG}, ethylene glycol volume.

^{a)}[M] refers to the moles of Cu per liter of the initial solution (CuCl₂·2H₂O dissolved in EG).

^{b)}w/w refers to the weight ratio of lignin, NaOH, or nucleating agent relative to elemental copper.

size and crystallite size decreased, reaching comparable values at the highest lignin concentration (L/Cu ratio of 9.8) and resulting in single-crystal particles, as shown in Figure S3, Supporting Information.

Trying to improve the yield to obtain larger amounts of sample, the effect of increasing the copper salt concentration from 0.5 to 1.8 M, at NaOH/Cu = 2.6 and L/Cu = 0.3 was successfully tested and resulted in a slight increase in particle size, from 230 to 270 nm (Figure S4, Supporting Information). Under these conditions, several syntheses were carried out using different types of organosolv lignins (SW, WS, and BW) to study the influence of lignin type on particle size. No significant influence on the size was observed by SEM, and similar hydrodynamic diameters were obtained for all particles with lignins from different sources (Figure S5a, Supporting Information). In the TGA analysis in an argon atmosphere (Figure S5b, Supporting Information), the particles with different lignin types showed a reduction in weight (<5%) upon heating, likely due to the decomposition of organic residues such as lignin or EG remaining on the nanoparticle surfaces. A greater weight reduction was observed in particles with SW lignin (B2L1), suggesting that these particles contained a slightly higher amount of lignin on their surface compared to the other types of lignin. Feedstock origin therefore only slightly affects the Cu particle synthesis and can be related to the variation in hydroxyl, aliphatic, phenolic, and

carboxylic hydroxyl group content in the lignins (Table S1, Supporting Information). In contrast, when using other lignins, Indulin AT and Alcell, derived from different pulping processes, under the same synthesis conditions, metallic copper particles were not formed; instead, a copper oxide phase was obtained in both cases with markedly different particle sizes (57 and 949 nm, respectively) (Figure S6, Supporting Information).

As a conclusion, the investigation of key parameters in the synthesis of Cu nanoparticles via a polyol process assisted by a batch microwave reactor enabled the identification of optimal conditions for scaling up to a continuous-flow microwave system. To improve the environmental sustainability of the method, the lowest effective NaOH/Cu ratio of 4.1, sufficient for forming metallic nanoparticles with and without lignin, was selected, and a Cu salt concentration of 0.5 M, which led to nanometer particle sizes, was also chosen. Furthermore, it was determined that small amounts of Fabiola lignin have a strong influence on the formation of metal copper nanoparticles, acting as a surfactant and being responsible for their good colloidal stability.

2.3. Large-Scale Synthesis of Cu NPs: Continuous-Flow Microwave

Metallic copper particles with a FCC crystalline structure were obtained in a microwave reactor operating in continuous flow at the optimal conditions, that is a NaOH/Cu ratio of 4.1 and a copper salt concentration of 0.5 M without additives, sample F (Table 2, Figure 3a). The resulting particles in continuous flow were 3.4 times larger than those obtained in batch microwave synthesis under the same concentration conditions (795 vs 84 nm). This size increase is primarily attributed to the difference in reaction times of the particles inside the reactor at the reaction temperature of 160 °C between both systems. In batch synthesis, the reaction time at this temperature is 10 min, whereas in continuous flow synthesis, it extends to 20 min. As a result, the prolonged residence time in the continuous flow microwave system leads to greater particle growth. It should be noted that in the continuous flow microwave system, the residence time is determined by the flow rates of the NaOH and copper salt solutions, which are controlled by peristaltic pumps. Reducing this residence time would require increasing the flow rates of the solutions, but this approach is limited by factors such as solution viscosity, pump capacity, and flow stability.

In order to reduce particle size, two strategies involving additives in the reaction medium were implemented: (1) increasing the amount of lignin, as previously done in the batch synthesis, and (2) introducing metal elements as nucleating agents, one (M) or a combination of multiple metals (MM), as described in Table 2. In all cases, within the tested additive concentrations (<10% molar or 15% w M/Cu), pure metallic copper particles with a FCC structure were obtained, with no secondary phases, as revealed by XRD (Figure 3b).

As expected, the size of the Cu NPs decreased with increasing lignin content up to a Lignin/Cu ratio of 3, as observed by SEM (from 795 to 75 nm) and by XRD (down to 56 nm) (Figure 3c,d). Lignin was found on the surface of the nanoparticles, as shown for the batch process, where it acted as a surfactant, limiting particle growth and leading to nanometric sizes. However, high lignin content may negatively affect conductivity. Therefore, alternative strategies were explored to further reduce particle size without compromising its surface and, consequently, the conductivity properties. The use of nucleating agents (e.g., Pt, Pd, and Ag) has been previously reported to induce heterogeneous

Table 2. Summary of reagent concentrations, volumes, and additives (Lignin and Metals) used in the continuous-flow microwave syntheses of Cu nanoparticles under various conditions. L, Lignin; M, Metal ions; MM, Multimetallic ions; V_{EG}, ethylene glycol volume.

Sample	Continuous-flow microwave synthesis								
	Cu Salt/Metals/Lignin + EG						NaOH+EG		
	Cu salt [M] ^{a)}	L	L/Cu (w/w) ^{b)}	M	M/Cu [w/w]	V _{EG} [mL]	NaOH [mmol]	V _{EG} [mL]	NaOH/Cu (w/w) ^{b)}
Cu synthesis									
F	0.5	—	—	—	—	200	600	600	4.1
FL1	0.5	SW	0.3	—	—	200	600	600	4.1
FL1.1	0.5	SW	3.1	—	—	200	600	600	4.1
Cu-M synthesis									
FM	0.5	—	—	Fe Lumps	0.13	200	600	600	4.1
FL1M	0.5	SW	3.1	Fe Lumps	0.13	200	600	600	4.1
Cu-MM synthesis									
FMM	0.5	—	—	Steel	0.17	200	600	600	4.1
FL1MM	0.5	SW	3.1	Steel	0.17	200	600	600	4.1

^{a)}[M] refers to the moles of Cu per liter of the initial solution (CuCl₂·2H₂O dissolved in EG).

^{b)}w/w refers to the weight ratio of lignin, NaOH, or metal nucleating agent relative to elemental copper.

nucleation in the polyol method.^[21] In this study, individual metal ions (Fe, Ni) were used as nucleating agents during the synthesis, each tested separately.

First of all, Fe ions from iron lumps were used as nucleating agents, leading to a ~78% reduction in average particle size (from 795 to 171 nm) and a more homogeneous size distribution, while XRD size decreased down to 75 nm (Cu-M, Figure 3c,d). Fe ions can act not only as nucleation sites, but also lowering the activation energy required for the formation of Cu nuclei. This process results in a higher number of nuclei forming during the initial stage, which in turn limits the growth of individual particles and reduces the final nanoparticle size. Additionally, the presence of small amounts of lignin further reduced the particle size to 137 nm. Despite the addition of 13 wt% metal Fe relative to Cu, only ~0.3 wt% Fe was detected in the final sample by EDX analysis. Other nucleating agents such as Fe(II) (Fe/Cu = 0.13) ions from FeCl₂ salt, also led to the formation of metallic copper particles, but only a small reduction in particle size was observed (562 nm) (Figure S7a,b, Supporting Information). In the case of Ni(II) (Ni/Cu = 0.03, 0.06, and 0.13) ions from NiCl₂ salt, the presence of copper oxide (Cu₂O) was detected (Figure S7b,c, Supporting Information) and it resulted in highly inhomogeneous particles with a wide particle size distribution, ranging from 90 nm to 2 μm.

Therefore, when using Fe lumps, these lumps dissolve in the initial copper salt and EG solution, leading to the oxidation of Fe⁰ to Fe²⁺ under standard conditions. Since Fe⁰ has a positive oxidation potential to Fe²⁺ (+0.447) and the reduction potential of Cu²⁺ is +0.342 V,^[33] iron can act as a spontaneous reducing agent. This enables the rapid reduction of Cu²⁺, either directly to metallic Cu⁰ or via an intermediate Cu⁺ species, which can subsequently be reduced to Cu⁰ as well. This process promotes fast and abundant nucleation during the subsequent alkaline polyol reduction, resulting in smaller and more uniform copper nanoparticles due to the increased number of initial nuclei. However, when Fe²⁺ (from FeCl₂) is used as a nucleating agent, it does not promote the reduction of Cu²⁺. The oxidation potential of Fe²⁺ is −0.771 V and no increase in the initial nucleation active sites occurs, allowing particles to grow larger before the copper precursor is

depleted. Some authors have reported the possibility of using Fe²⁺ as a green reducing agent for the rapid synthesis of gold nanoparticles.^[34] In that case, Fe²⁺ reduced gold ions (Au³⁺) to metallic gold (Au⁰) due to a favorable difference in their standard reduction potentials. In the case of Ni²⁺, it has a more negative reduction potential of −0.257 V than Cu²⁺; therefore, like Fe²⁺, Ni²⁺ does not promote the reduction of Cu²⁺.

Further reduction in particle size below 100 nm was obtained using multimetallic nucleating agents such as SS316Ti steel primarily consisting of iron (65–70%), with chromium (≈17%), nickel (≈10–14%), and small amounts of titanium (0.5–1%) and molybdenum (2–3%). This steel dissolved completely in the solution containing copper chloride, ethylene glycol, and lignin. Metal copper nanoparticles of 72 nm were obtained, and, upon the addition of lignin, this size decreased to 47 nm, which is in good agreement with the XRD size of 45 nm (FL1MM, Figure 3c). The presence of these elements in the synthesis can simultaneously act as reductants and nucleating sites, enhancing the nucleation rate and limiting particle growth. In particular, the presence of Fe⁰ promotes the reduction of Cu²⁺ to Cu⁰ or Cu⁺, while Ni and Cr contribute additional nucleation centers, leading to the formation of a larger number of smaller nanoparticles.

A reduction in the hydrodynamic diameter of the particles was observed with the increasing concentration of lignin during synthesis using the continuous-flow microwave reactor (Figure 3e, F: 481 ± 159 nm, FL1: 406 ± 90 nm, FL1.1: 372 ± 111 nm, FM: 466 ± 40 nm, FL1M: 290 ± 84 nm, FMM: 313 ± 47 nm, FL1MM: 242 ± 22 nm). Additionally, a further decrease was also evident with the use of nucleating agents, particularly when multimetallic nucleating agents were introduced. These findings highlight the combined effect of lignin and nucleating agents in promoting finer particle formation by enhancing nucleation and limiting particle growth. On the other hand, an organic content of <2% was determined for the particles synthesized without lignin, as measured by TGA analysis under argon atmosphere (Figure 3f). This residual organic content is attributed to the presence of EG adsorbed on the particle surface. When lignin was added at a L/Cu ratio of 3.1, the organic content increased to ~3%.

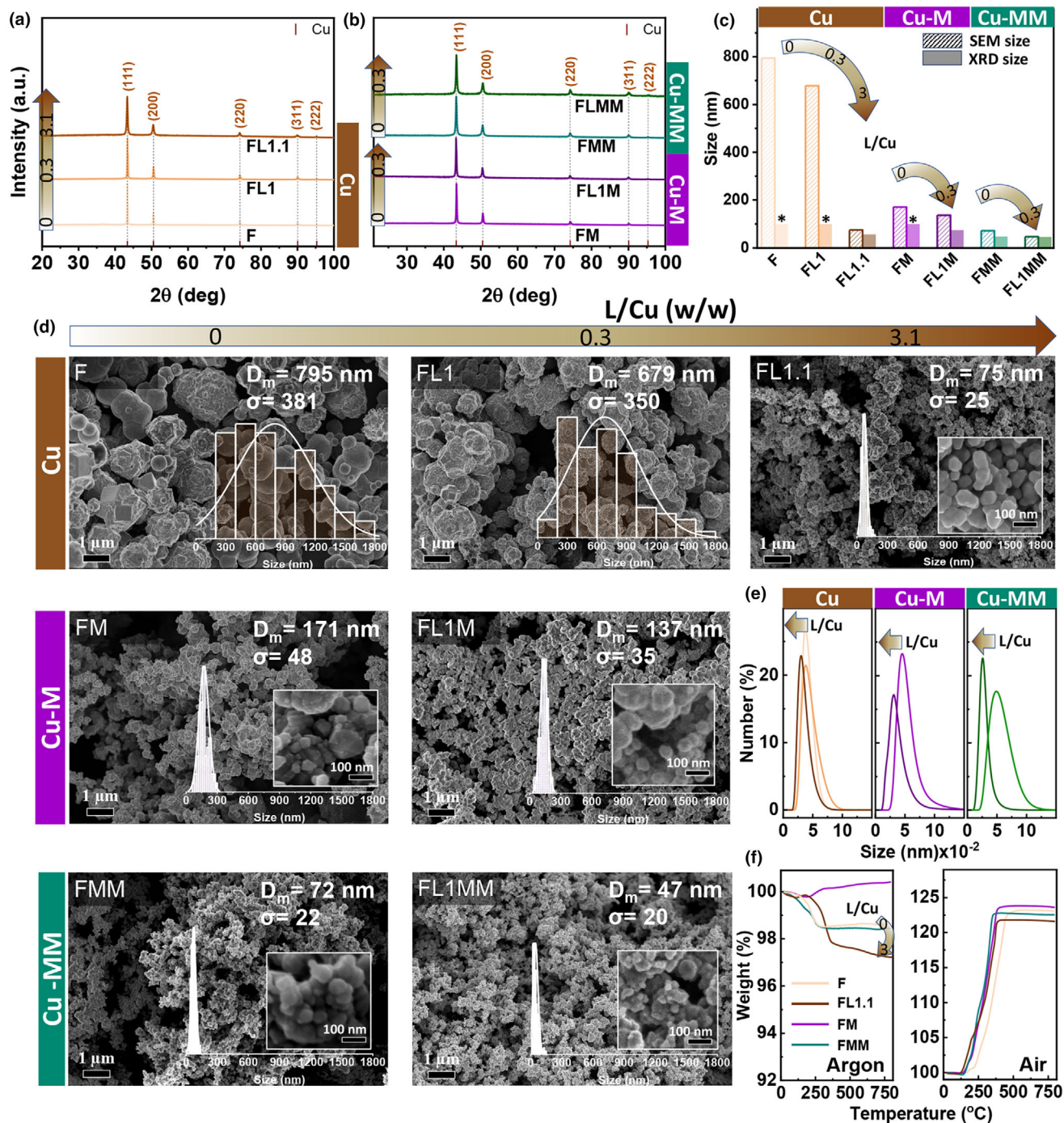


Figure 3. Chemical and structural characterization of Cu NPs synthesized by the microwave-assisted polyol process in continuous-flow (F) described in Table 2. a, b) XRD diffractograms measured for Cu NPs obtained without additives and in the presence of lignin (FL), metal nucleating agents (FM, FMM) or both (FLM); c) Influence of lignin content and metal nucleating agents used during synthesis on the crystallite and particle size of Cu NPs measured by XRD and SEM. *Crystallite sizes >100 nm. d) SEM images, e) Hydrodynamic diameter in EG medium measured by DLS and f) Thermogravimetric analysis in Argon of Cu NPs obtained using different nucleating agents and different Lignin/Cu ratios.

Furthermore, consistent with the results obtained from batch microwave synthesis, the TGA analysis performed in air revealed the onset of copper oxidation above $\sim 145^{\circ}\text{C}$, evidenced by a mass gain of approximately 20–25%, which corresponds to the conversion of metallic copper into copper oxide.

2.4. Surface Characterization of Cu NPs by HR-STEM

The correlation between macroscopic measurements, microstructure, and nanostructure of Cu NPs synthesized in this study was investigated using HR-STEM for selected samples with particle sizes below 100 nm

(Figure 4). Three representative cases were considered to study composition and structure at the atomic scale: the effect of metal nucleating agents (FMM; 72 nm), high lignin concentration (FL1.1; 75 nm), and the combined effect of lignin and metal nucleating agents (FL1MM; 47 nm). Additionally, commercial nanoparticles treated with EG (CnEG; 40 nm) were included for comparison. These cases allowed the evaluation of the effects of nucleating agents, lignin content, and their combination on the final structure and composition of the nanoparticles.

The effect of using nucleating agents is shown in Figure 4a–d, confirming the narrow size distribution and nanoscale nature of FMM. In this case, the absence of a Cu oxide layer is evident in Figure 4b, where no core–shell structure can be observed. This is further supported by Figure 4c, where both the outer and inner regions display a Cu $L_{2,3}$ edge characteristic of metallic Cu.^[35] EELS analysis presented in Figure S8, Supporting Information reveals that the FMM contains approximately 3% nickel and 1% iron, coming from the multimetallic nucleating agents (stainless steel) used during synthesis. These elements are incorporated into the Cu structure during the nucleation and growth process and may also act at the surface, preventing the oxidation.^[3] Additionally, Figure 4d reveals a carbon distribution surrounding the Cu NPs, attributed to residual EG from the synthesis process.

In Figure 4e–h, the nanoparticles prepared with the highest L/Cu ratio (L/Cu = 3.1) (sample FL1.1) show an atomic-resolution HAADF-STEM image, where the edge of the Cu NPs is observed as well as an oxide layer. Atomic resolution of the Cu_2O layer can be seen, further evidenced in Figure 4g, where two EELS spectra, corresponding to the inner and outer regions of the Cu NPs, are presented. The EELS spectrum reveals a mixture of the Cu $L_{2,3}$ edge for Cu_2O and metallic Cu, with a more pronounced presence of the oxidized state at the Cu NP's edge.^[36] Additionally, Figure 4h shows the EELS distribution of C, Cu, and O, highlighting a uniform presence of C and O throughout the entire NP, with a higher concentration in the outer region. This confirms the presence of lignin on the NP surface.

Sample FL1MM (Figure 4i–l) is formed by nanoparticles with an atomic arrangement that corresponds to a FCC Cu lattice, which remains coherent even at the NP's edge, as shown by the atomic-resolution HAADF-STEM image of a NP (Figure 4j). The inset shows the fast Fourier transform (FFT) of the red-dotted area and confirms the cubic arrangement in the $[111]$ direction, parallel to the electron beam. Figure 4k presents the annular dark-field (ADF) intensity profile of a NP. Since the O K edge was not detected in the line scans across the NP, an averaged Cu $L_{2,3}$ spectrum with a 10 nm step along

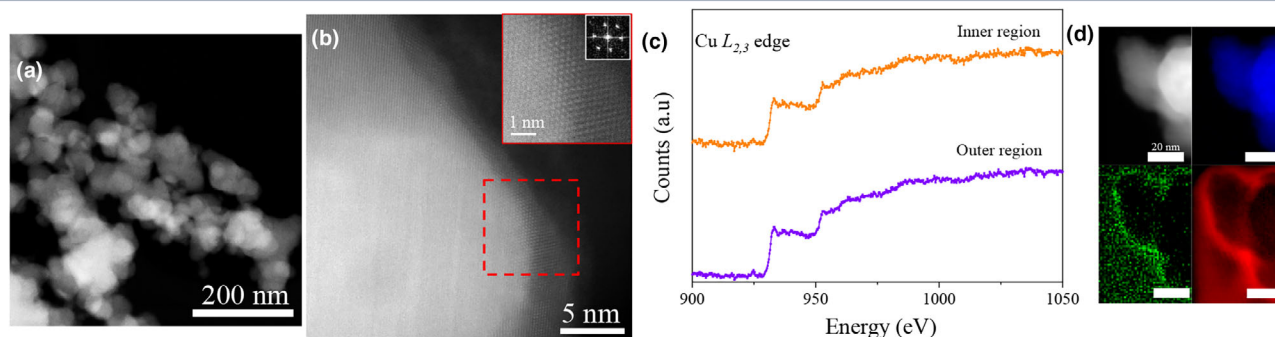
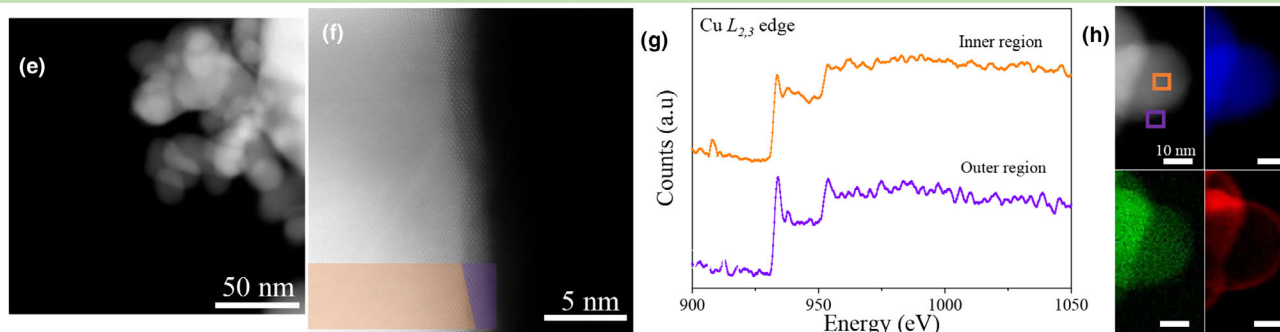
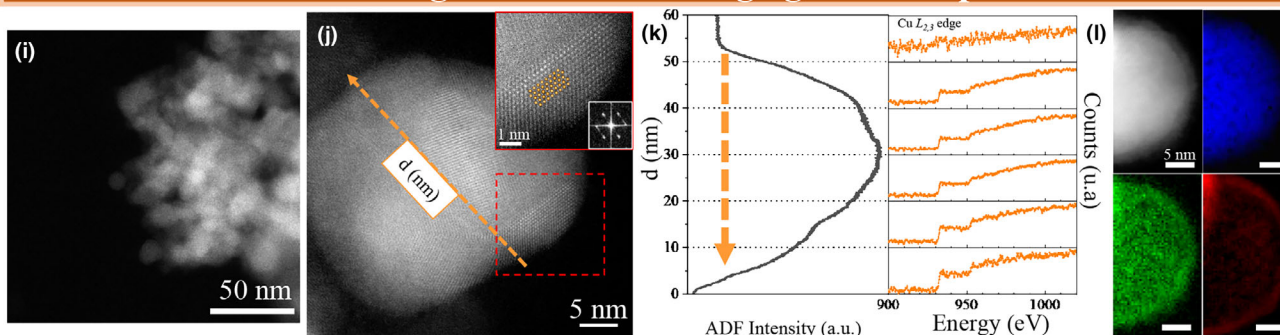
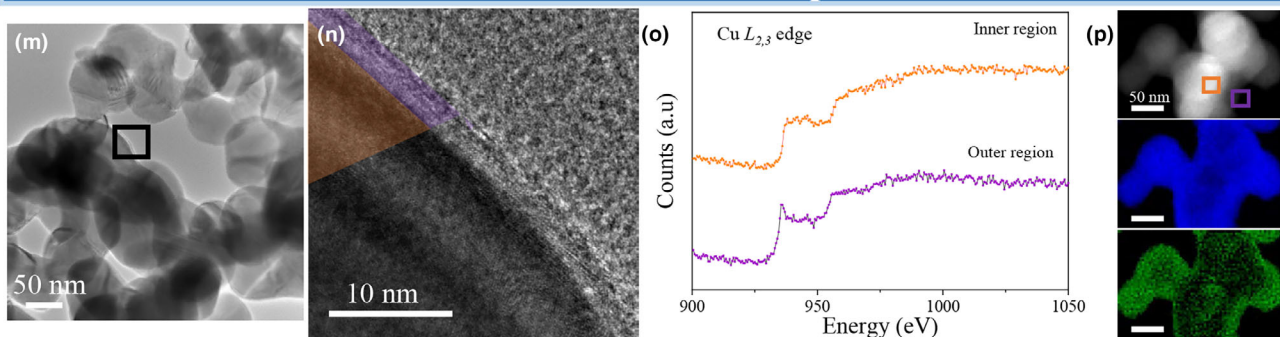
the NP is displayed. From 0 to 50 nm, the Cu $L_{2,3}$ edge does not exhibit any oxidized features, confirming the metallic state of the nanoparticles.^[36] Notably, the last spectrum (50–60 nm) corresponds to the NP's extremity and presents a noisy signal. Additionally, Figure 4i shows the EELS distribution of C, Cu, and O. The uniform presence of C and O across the entire NP is observed, with a higher concentration in the outer region, confirming the persistence of organic coating (lignin and EG) on the NP surface. EELS analysis did not reveal the presence of any metallic element other than Cu.

Finally, the structural composition of the commercial nanopowders after EG treatment (Figure 4k,m) was also examined by HR-STEM. Figure 4n presents a magnification of the black square region in Figure 4m, where a HAADF-STEM image of the Cu NP edge is shown. In this image, the oxide layer is colored in purple, while the inner region, colored in orange, corresponds to FCC Cu. These regions – Cu_2O and FCC Cu– are further evidenced in Figure 4o, where two EELS spectra, corresponding to the inner and outer regions of the Cu NPs, are presented. The EELS spectrum reveals a mixture of the Cu $L_{2,3}$ edge for Cu_2O and metallic Cu, with the oxidized state being more pronounced at the Cu NP edge.^[36] Additionally, the EELS distribution of Cu and O is shown in Figure 4p. In contrast, HR-STEM images of this sample before EG treatment (Sample Cn) showed a higher concentration of oxygen in the outer regions that correspond to a thicker copper oxide shell, further validated by the Cu edges observed in the EELS analysis (Figure S9, Supporting Information).^[37] Turbostratic carbon is observed surrounding the NPs for sample Cn. This form of carbon, characterized by disordered graphene layers, may serve as an effective protective barrier,^[38] similar to the oxide layers that commonly form on metals, serving as a protective barrier that inhibits corrosion.^[39]

2.5. Productivity, Reproducibility, and Long-Term Stability

To evaluate the efficiency and scalability of the synthesis process, productivity was assessed in terms of grams of product obtained per hour (g h^{-1}). In the case of the microwave-assisted synthesis performed in batch mode, using a copper salt concentration of 0.5 M, 0.1 g of nanoparticles was produced per batch in 30 min, corresponding to a productivity of $\sim 0.2 \text{ g h}^{-1}$. To increase the yield of metallic Cu nanoparticles under the same batch conditions, the copper salt concentration was raised to 1.8 M. Under these conditions, 0.5 g of nanoparticles was obtained per batch, resulting in a productivity of $\sim 1 \text{ g h}^{-1}$. However, it is important to note that under these conditions ($\text{NaOH/Cu} = 2.6$), metallic copper particles were not formed in the

Figure 4. HR-STEM study of nanoparticles with sizes smaller than 100 nm. Sample FMM: a) HAADF-STEM image. b) Atomic-resolution HAADF-STEM image. The inset displays the atomic FCC lattice oriented in the $[111]$ direction, as confirmed by the FFT. c) Two ADF intensity profiles. Linescans correspond to the Cu $L_{2,3}$ edge averaged inner and outer regions of Cu NP to show the Cu oxidation state distribution. d). From left to right: ADF-STEM image, 2D SI false-colored maps obtained from EELS, specifically Cu $L_{2,3}$ (blue), O K (green), and C K (red) edges. Sample FL1.1: e) HAADF-STEM image. f) Atomic-resolution HAADF-STEM image. g) Two ADF intensity profiles. Linescans correspond to the Cu $L_{2,3}$ edge averaged from the square regions in f) to show the Cu oxidation state distribution. h) From left to right: ADF-STEM image, 2D SI false-colored maps obtained from EELS, specifically Cu $L_{2,3}$ (blue), O K (green), and C K (red) edges. Sample FL1MM: i) HAADF-STEM image. j) Atomic-resolution HAADF-STEM image. The inset displays the atomic FCC lattice oriented in the $[111]$ direction, as confirmed by the FFT. k) ADF intensity profile. Linescans on the right panel correspond to the Cu $L_{2,3}$ edge averaged every 10 nm along the nanoparticle to show the Cu oxidation state distribution. l) From left to right: ADF-STEM image, 2D SI false-colored maps obtained from EELS, specifically Cu $L_{2,3}$ (blue), O K (green), and C K (red) edges. Sample CnEG: m) HAADF-STEM image. n) Atomic-resolution HAADF-STEM image. o) Two ADF intensity profiles. Linescans correspond to the Cu $L_{2,3}$ edge averaged from the square regions in n), displaying a metallic FCC Cu signature (orange) and a Cu_2O signature (purple). p) From left to right: ADF-STEM image, 2D SI false-colored maps obtained from EELS, specifically Cu $L_{2,3}$ (blue), O K (green), and C K (red) edges.

Nucleating agents influence: sample FMM**High lignin concentration influence: sample FL1.1****Combination of lignin and nucleating agents: sample FL1MM****Commercial EG treated: sample CnEG**

absence of lignin; instead, a copper oxide phase was observed (Figure S4a, Supporting Information). In contrast, in the presence of lignin, metallic particles were successfully obtained, although they exhibited larger sizes (~230–270 nm). For the batch

microwave-assisted synthesis of Cu nanoparticles, a reaction efficiency greater than 85% was achieved.

With the aim of scaling up the process and increasing the productivity of Cu nanoparticles, the synthesis was transferred to a

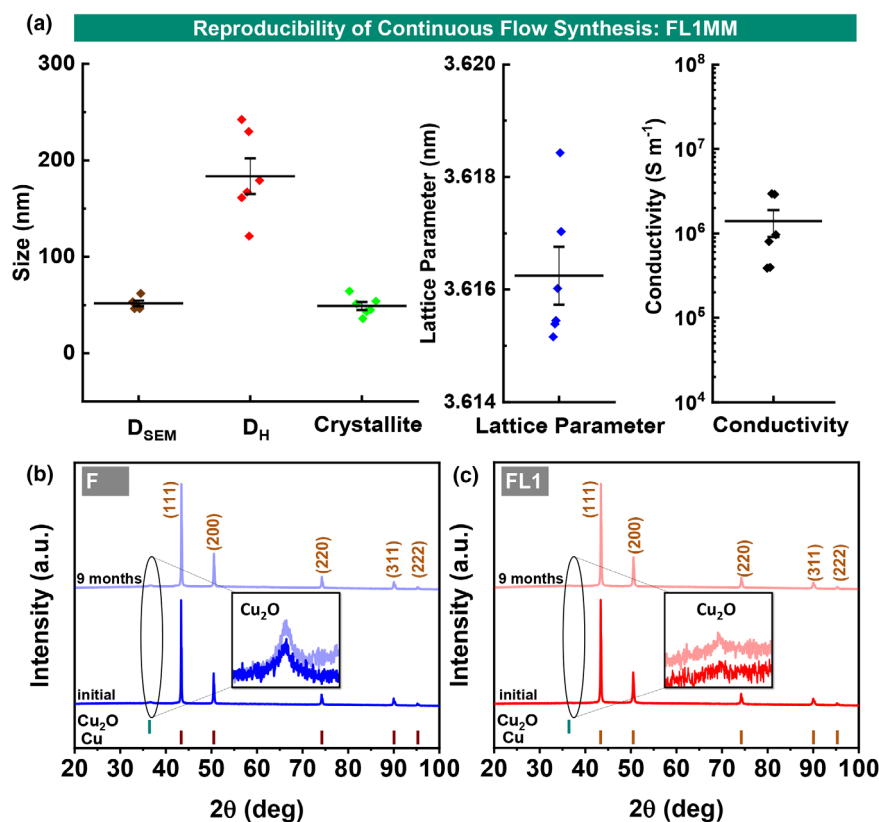


Figure 5. a) Reproducibility study evaluated through key parameters including nanoparticle size, hydrodynamic diameter, crystallite size, lattice parameter, and electrical conductivity. Stability in air of copper nanoparticles prepared by the continuous flow process b) with and c) without lignin (Samples FL1, F) followed by XRD during 6 months.

continuous-flow microwave reactor. In continuous flow mode, a productivity of 3.4 g h^{-1} was achieved, which is more than three times higher than that obtained in batch mode. Additionally, the reaction efficiency improved significantly, exceeding 95%. The reproducibility of this synthesis was evaluated by analyzing key parameters such as nanoparticle size, hydrodynamic diameter, crystallite size, crystal lattice parameter, and electrical conductivity (Figure 5a). These metrics provided a comprehensive assessment of the consistency of the synthesis process and the quality of the resulting copper nanoparticles across six different batches.

The stability of the particles over a nine-month period and the influence of lignin on this stability were studied using particles with and without lignin (Samples FL1 and F), synthesized in the continuous-flow microwave reactor. The appearance of a peak at low 2θ angles in sample F (Figure 5a) indicates the presence of copper oxide from the beginning, which increases very slightly during the studied period. However, despite this slight increase, the percentage of copper oxide phase remains below 1.5%, estimated from the XRD analyses. On the other hand, the XRD patterns for sample FL1 do not exhibit oxide phases such as Cu₂O and CuO during the studied period (Figure 5b). This confirms that the metallic copper nanoparticles stabilized with lignin remained stable during storage, showing no signs of oxidation or degradation over time.

2.6. Electrical Conductivity and Sintering Characterization of Cu Nanoparticles

Characterization of the electrical properties of the copper particles synthesized in this study was done after sintering to ensure the effective formation of electrically conductive circuits through the nanoparticles. Two sintering processes were tested: i) compressing the dry powder in pellets and ii) heating a strip-shaped sample, as described in the experimental section. In the first case, particles obtained from batch and continuous-flow microwave syntheses, as well as commercial Cu particles, were used for comparison. In the second case, a conductivity study was carried out at different sintering temperatures. For this purpose, a strip-shaped sample was prepared by depositing a dispersion of nanoparticles in EG (20 wt %). The selected sample for these experiments was B2L1, with a mean particle size of 271 nm ($\sigma = 120 \text{ nm}$) and 5% organic content. It should be taken into account that in order to get continuous conductive pathways, particles must meet stringent quality criteria such as high purity, freedom from copper oxides, and contain minimal amounts of turbostratic or amorphous carbon or organic coatings. These impurities can inhibit the sintering process and compromise the chemical stability of the material under sintering conditions.^[40]

The pellet-based approach enabled a comparative analysis of the electrical conductivity of all Cu nanoparticles prepared in this work and commercial powders before and after coating

with EG. Samples prepared using this method are expected to exhibit an increase in electrical conductivity upon sintering due to the formation of larger, interconnected structures. To study this effect, SEM images were acquired from the surface and cross-section of pressed pellets and are illustrated in Figure 6a for sample FL1MM. The low-magnification SEM image from the surface reveals micrometer-scale inhomogeneities, clearly visible at higher magnification, showing the presence of incomplete conductive pathways, some regions remain insufficiently interconnected. A similar behavior is observed in the cross-section of the pellet (Figure 6a), where no apparent defects are visible at low magnification, but at high magnification, inhomogeneities appear, confirming that complete sintering has not been achieved throughout the pellet, and large agglomerates can still be observed.

In Figure 6b, the electrical conductivities of the pellets from Cu NPs synthesized via a microwave-assisted polyol process in batch (B2L2) and Cu particles synthesized in continuous flow using different lignin concentrations (F, FL1, FL1.1) and nucleating agents (FL1M, FL1MM) are illustrated. Commercial Cu particles without (Cn, Cm) and with EG coating treatment (CnEG, CmEG) are included for comparison. EG coating is used to reduce the amount of oxide at the commercial particle surface (Figure S10a–d, Supporting Information), according to our earlier studies for other metallic nanoparticles.^[15] As already mentioned, CuO can act as an insulating layer, which negatively affects the electrical conductivity of the material.^[41]

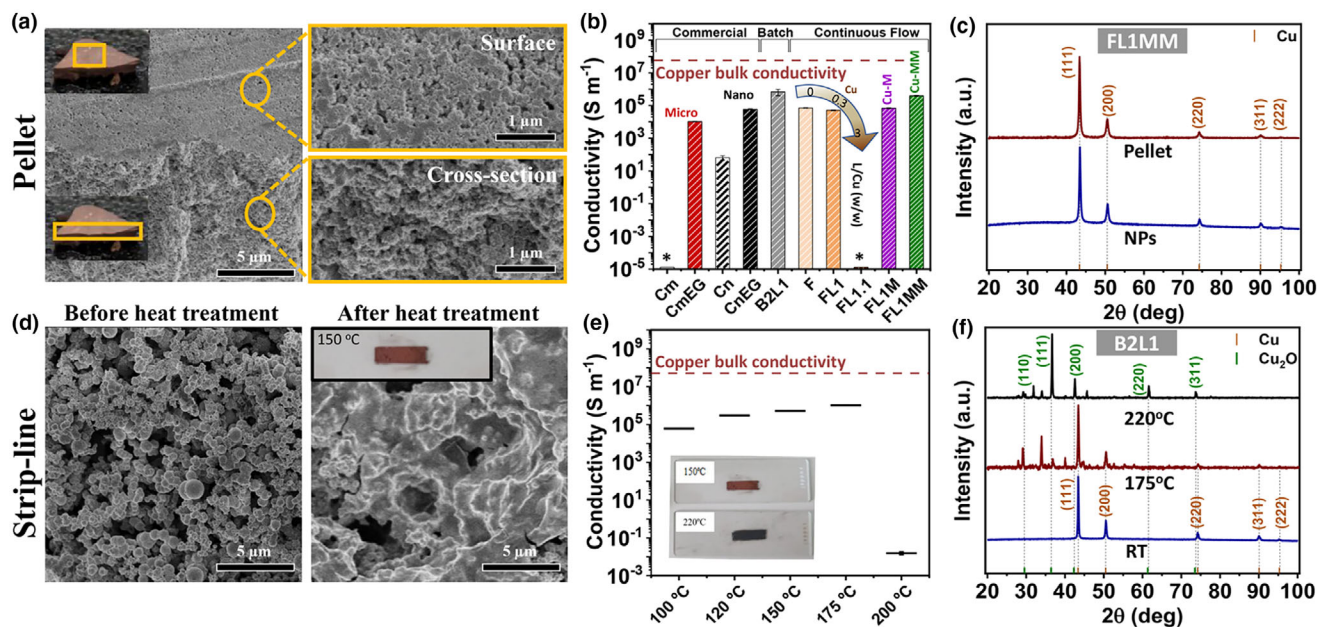


Figure 6. a) SEM images of the surface and cross-section of the pellet prepared from sample FL1MM. The insets show photographs of the pellet section analyzed mounted on the SEM holder, with regions of interest indicated by yellow squares; b) Electrical conductivity of the pellets from commercial Cu nanoparticles without (Cn, Cm) and with EG (CnEG, CmEG), Cu NPs synthesized via a microwave-assisted polyol process in batch (B2L2), and Cu particles synthesized in continuous flow using different lignin concentrations (F, FL1, FL1.1) and nucleating agents (FL1M, FL1MM); c) XRD patterns for sample FL1MM before (NPs) and after 3-ton pressing (pellet); d) SEM images of a strip line fabricated from sample B2L1, before and after heat treatment; e) Conductivity measurements of the strip-line (fabricated from B2L1 nanoparticle) after heat treatment at different temperatures; f) XRD profiles of the strip-line (fabricated from B2L1 nanoparticle) after heat treatment at different temperatures, showing complete oxidation at 220 $^{\circ}\text{C}$. *Conductivity was not detected due to the high resistivity of the sample. Copper bulk conductivity is $5.8 \times 10^7 \text{ S m}^{-1}$.

Initially, all untreated powders exhibited no electrical conductivity. However, after undergoing pressure processing, a significant enhancement in conductivity was observed in nearly all samples. In the case of the untreated (with EG) commercial particles (Cn, Cm), high resistivity was observed due to the presence of an oxide layer on their surface, which in some cases hindered the conductivity measurements. However, after treatment to remove this oxide layer and subsequent application of pressure, enhanced conductivity was observed. This result agrees well with the partial sintering observed by SEM for most of the particles (Figure 6a), except for commercial micrometer particles that retained their individual morphology, even after being subjected to 3 tons of pressure (Figure S10a, Supporting Information). The samples prepared in this work achieved electrical conductivities in the range of 10^5 to 10^6 S m^{-1} , approaching the conductivity of bulk FCC copper ($5.8 \times 10^7 \text{ S m}^{-1}$, defined by IACS International Annealed Copper Standard). Lower conductivity can be attributed to incomplete sintering and the presence of carbon residues.^[42,43] The oxidation layer is expected to be minimal for Cu NPs synthesized via microwave-assisted polyol methods, both batch and continuous processes, given the XRD data (Figure 6c). Correspondingly, pellets made from these nanoparticles show higher electrical conductivity than CnEG, suggesting better sintering and interparticle connectivity. In the case of commercial nanoparticles, although EG treatment removes copper oxide and restores conductivity to $\sim 10^5 \text{ S m}^{-1}$ in CnEG, SEM images show only partial sintering (Figure S11b, Supporting Information). Analyzing the role of the additives, Cu nanoparticles synthesized via microwave-assisted continuous flow showed a marked decrease in electrical conductivity with increasing lignin content. The high lignin

content (L/Cu ratio of 3) in sample FL1.1 hindered the conductivity measurement. This organic layer hinders sintering and disrupts conductive pathways, reducing electron transport. In contrast, nanoparticles synthesized with both lignin and multiple metal ions (FL1MM) exhibited significantly higher conductivity ($\sim 10^6 \text{ S m}^{-1}$), despite a much lower average particle size, 47 nm (Figure 6b). This suggests that low levels of Ni and Fe do not disrupt the metallic connectivity within the Cu NPs. Our results demonstrate the trade-off between oxide layer content and sintering efficiency, where an excessively thick oxide layer prevents the formation of conductive pathways between NPs. Similarly, the difference in sintering behavior between FL1MM and FL1.1 highlights that a large amount of organic material can also hinder sintering between NPs, even in the absence of a thick oxide layer.

On the other hand, the strip-shaped approach enabled an analysis of electrical conductivity at different sintering temperatures. SEM images of the strip-line before heat treatment show well-defined, isolated Cu nanoparticles (Figure 6d). During thermal treatment in air at 150 $^{\circ}\text{C}$, the particles start to form larger metallic copper structures, as seen in Figure 6d (after heat treatment). This transformation indicates the sintering-driven consolidation of the nanoparticles into an interconnected network, improving both structural integrity and electrical conductivity.^[40,44] In agreement with this, conductivity begins only after reaching 100 $^{\circ}\text{C}$, increasing markedly, from $6 \times 10^4 \text{ S m}^{-1}$ to $1 \times 10^6 \text{ S m}^{-1}$, after heating from 100 to 175 $^{\circ}\text{C}$ (Figure 6e). This increase is mainly due to improved sintering as observed by TEM. At 100 $^{\circ}\text{C}$, Cu nanoparticles form weak bonds, but conductive pathways remain limited due to incomplete sintering.^[28] As the temperature reaches 175 $^{\circ}\text{C}$, sintering becomes more effective, strengthening

interparticle bonds and improving contact, which leads to continuous conductive paths and significantly lower resistance. However, with the temperature increase in an air atmosphere, partial oxidation of the sample also begins to occur, progressing up to 220 °C, where the sample becomes fully oxidized (Figure 6f) and its conductivity drops sharply ($2 \times 10^{-2} \text{ S m}^{-1}$).

The typical sintering temperature of bulk copper is around 850–1000 °C in a reducing or inert atmosphere (e.g., hydrogen or argon).^[45] In air, sintering at these temperatures is not feasible due to rapid oxidation of copper. For nanoparticle-based copper, sintering can occur at much lower temperatures (e.g., 150–250 °C) due to the higher surface energy and diffusivity of nanoscale materials.^[46] Similar results have been found for other materials such as silver and gold nanoparticles, reaching high conductivities of 10^4 S m^{-1} at low heating temperatures (100–300 °C).^[47] In general, copper nanoparticle films sintered under reducing conditions or with external energy sources that allow fast and localized heating (laser, plasma, photonic) show good conductivity, approaching 10 to 30% of bulk copper, $\sim 10^5$ – 10^6 S m^{-1} ,^[3] similar to the values obtained in this work using conventional thermal sintering in air.

Finally, the colloidal stability of lignin-coated copper nanoparticles (B2L1, FL1MM) in a formulated ink containing 50 mgNP mL⁻¹, was assessed using a Turbiscan Lab optical analyzer and compared with the commercial nanopowders subjected to EG treatment (CnEG) (Figure S12, Supporting Information). The Turbiscan® Stability Index (TSI), which is inversely correlated with suspension stability, was reduced by half in the case of FL1MM relative to B2L1, most likely due to the decrease in particle size, and reached values comparable to those of the CnEG sample. This enhanced stability under concentrated conditions is particularly relevant for future applications in conductive ink formulations.

3. Conclusions

This work demonstrates that microwave-assisted polyol synthesis enables the continuous production of metallic copper nanoparticles, with tunable sizes ranging from 40 to 800 nm. This approach ensures high reproducibility and eliminates batch-to-batch variation, enabling scalable synthesis at a rate of approximately 5 g h^{-1} . Beyond particle size control, the method also enhances surface reduction and improves dispersion stability provided by the polyol rest at the nanoparticle surface. It should be highlighted the versatility of Cu-based nanoparticles for electronics, optics, sensors, catalysts, and medical applications,^[48] far beyond traditional applications. They are cost-effective alternatives to noble metal catalysts, used for example in hydrogenation, oxidation, and C-C coupling reactions^[1] and for electrochemical CO₂ and CO reduction, selectively producing alcohols such as ethanol and propanol.^[49]

The strategy proposed here addresses the major limitation of copper nanoparticles, their susceptibility to oxidize, by introducing lignin into the reaction medium. The presence of adsorbed lignin and metal nucleating agents serves as a protective layer that shields the NPs from oxidation. This passivation layer blocks the diffusion of oxygen to the Cu surface, inhibiting the formation of oxide phases. Over extended periods, such as 9 months, this passivation proves crucial in maintaining the structural and compositional stability of the NPs. Lignin offers important advantages over other additives such as PVP given its thermal properties. It has been shown here that the glass transition temperature

goes from 124 °C down to 100 °C when lignin is bound to the nanoparticle surface; that is the temperature at which lignin transforms from hard to soft rubbery state, allowing mobility of the polymer chains (melt blending). In addition, the decomposition temperature takes place at lower temperature (<200 °C) in comparison to PVP (250 °C). These thermal softening effects facilitate processing by enabling the formation of percolation pathways at low temperatures, which leads to high conductivity in the printed patterns.

In agreement with this, it was demonstrated that nanometer-size copper particles were capable of sintering under low-energy conditions. Our experimental data indicate that low-energy sintering is also possible with bigger copper nanoparticles if the surface is free from oxides and contains minimal organic residues. Conductivities of $\sim 10^6 \text{ S m}^{-1}$ (100 – $30 \mu\Omega\text{-cm}$) were obtained by using pressure or low temperatures, such as 150 °C (compatible with heat-sensitive substrates such as plastic) for sintering. These values could be significantly improved by optimizing the sintering process, for example, by adjusting temperature, time, or atmospheric conditions. Such improvements would enhance particle connectivity and electrical performance, making these nanoparticles more suitable for use in conductive inks aimed at producing more sustainable and efficient printed circuits.

4. Experimental Section

Materials: Commercial samples of metal copper micro- and nanoparticles, with particle sizes above microns and below 100 nm, respectively, were purchased from Thermo Scientific Alfa Aesar and Merck Corp. with the following references: 042455.18 and CU-M-02 M-NP.100 N, respectively. Copper (II) chloride dihydrate ($\text{CuCl}_2 \cdot 2\text{H}_2\text{O}$, 99%), iron (II) chloride anhydrous (FeCl_2 , 98%), nickel (II) chloride anhydrous (NiCl_2), sodium hydroxide (NaOH, 98%), ethylene glycol (EG, $\text{C}_2\text{H}_6\text{O}_2$, 99%) and anhydrous methanol (99.8%), which were obtained from the US company Sigma-Aldrich. Iron lumps (99.98%) (metallic solid Fe) were obtained from Johnson Matthey, UK, and Stainless Steel 1.4571 (316Ti) bar from Stainless Europe. All chemical reagents were used without further purification. The lignins used in the synthesis were extracted from various plant sources, including spruce wood (SW), wheat straw (WS) and beech wood (BW) named as L1, L2, and L3, respectively. Beech wood lignin, partially depolymerized (L4), has also been utilized. These lignins were obtained by a three-step aqueous acetone organosolv pulping under acidic conditions (a modification of the so called Fabiola process).^[50] For comparison, Indulin AT and Alcell lignins derived from different pulping processes (Kraft pulping of softwood and water/ethanol organosolv pulping of hardwood) were used. The main characteristics of the lignins used in this study, including hydroxyl group content and molecular weight, are summarized in Table S1, Supporting Information.

Cu NPs batch microwave synthesis (sample B)—Cu NPs were synthesized via a microwave-assisted polyol process using a Monowave 450 reactor (Anton Paar GmbH). $\text{CuCl}_2 \cdot 2\text{H}_2\text{O}$ was dissolved in EG under magnetic stirring (Samples B1–B2), and lignin was added in some experiments under specific conditions (Samples L1–L4). Separately, a NaOH solution in EG was prepared at 140 °C with magnetic stirring. The two solutions were then combined and introduced in the microwave. Full reaction conditions are summarized in Table 1. Inside the microwave reactor (Figure 1a), samples were first heated to 70 °C and held for 10 min, and then further heated to 160 °C for another 10 min with magnetic stirring at 800 rpm (Figure 1c). After the reaction, the mixture was cooled to 55 °C. The product was divided into aliquots and centrifuged at 4000 rpm for 1 h. The precipitate was washed three times with methanol, each time centrifuging at 4000 rpm for 10 min. The final material was dried under vacuum at room temperature.

Cu NPs continuous-flow microwave synthesis (sample F)—The continuous-flow synthesis of Cu NPs was carried out using the CEM DISCOVER 2.0 microwave reactor. $\text{CuCl}_2 \cdot 2\text{H}_2\text{O}$ was dissolved in EG at 80 °C under magnetic stirring. Other additives, such as lignin or metal ions, were incorporated under specific conditions and samples were named as a function of the absence (Sample F) or

the presence of these agents (L for lignin and M for one metallic ion, MM for multimetallic ions). The specific conditions for each synthesis are provided in Table 2. Additionally, a solution of EG with NaOH was prepared at 130 °C under magnetic stirring in the glove box. Both solutions were fed separately into the microwave reactor (Figure 1b) using two peristaltic pumps (Teledyne ISCO, PeriXus®). The NaOH solution was delivered at 7.2 mL min⁻¹ and the copper salt solution at 2.4 mL min⁻¹, maintaining a continuous flow through the reactor and achieving a residence time of 20 min. The reaction was conducted at 160 °C with mechanical stirring at 450 rpm (Figure 1d). After the reaction, the product was separated from the mother solution by centrifugation at 4000 rpm for 1 h, washed three times with methanol (centrifuging at 4000 rpm for 10 min each), and dried under vacuum at room temperature.

Coating process for Cu commercial powders (sample C)—The coating process of commercial samples of metal copper micro- and nanoparticles (Samples Cm and Cn) using EG in a strong alkaline medium and at high temperature was adapted from the polyol synthesis method for metal particles, replacing the copper precursor with commercial powder (Samples CnEG and CmEG). A suspension of particles (0.4 M) in EG and NaOH (1.75 M) (previously dissolved at 90 °C and then cooled before adding the metal NPs) was prepared in a glove box under oxygen-free conditions. This suspension was then pumped into the microwave reactor (CEM Discover 2.0). The pumping rate was adjusted to obtain a residence time inside the microwave of 1 h at 175 °C.

Samples characterization: Powder X-ray diffraction characterization (PXRD)—The crystal structure of the samples was determined using Powder X-ray diffraction, with data collected on a Bruker D8 Advance Davinci diffractometer in Bragg–Brentano configuration for powder samples. The measurements were performed using Cu K α radiation, specifically K α_1 (λ = 1.54060 Å), K α_2 (λ = 1.54443 Å), and K β (λ = 1.39225 Å). For each sample, a portion of the dried powder was mounted on a zero-diffraction plate for analysis. The scan covered a 2 θ range from 20° to 100° to capture all relevant diffraction peaks, particularly those associated with metal phases and potential oxide formations.

Crystal structure refinement was carried out using GSAS-II, utilizing CIF files from the PDF database. The refinement employed PDF Card 00–004–0836 for Face-Centered Cubic (FCC) Cu and PDF Card 00–005–0667 for FCC Cu₂O, confirming the presence of these phases. The crystallite size (D) and lattice parameters of the Cu NPs were extracted from the refinement results. Crystallite size was estimated using the Debye–Scherrer equation, which relates XRD peak broadening to crystallite dimensions. The full width at half maximum (FWHM) of the diffraction peaks was analyzed to approximate the coherent diffraction domain size. To correct for instrumental broadening, a silicon (Si) standard was used to generate an instrumental response function (IRF) file.

Electron microscopy analyses—High-Angle Annular Dark-Field Scanning Transmission Electron Microscopy (HAADF STEM) analysis was carried out in a JEOL JEM-ARM 200CF microscope, equipped with a CEOS spherical aberration corrector and a Gatan Quantum Electron Energy Loss (EEL) spectrometer, operated at 200 kV. Aberration-corrected Z-contrast (HAADF) images provide atomic-resolution contrast based on atomic number.

SEM analysis was conducted to examine the surface morphology and structural characteristics of the samples. The SEM was operated at an accelerating voltage of 5 kV, and images were acquired at various magnifications to assess the surface texture, particle distribution, and other microstructural features. The sample preparation varied depending on whether powder, pressure-sintered pellets, or heat-sintered particles were measured. For NPs, a solution was deposited onto a silicon substrate on the SEM holder with carbon tape and allowed to dry. The size of more than 150 particles was measured, and the histogram was fitted using a normal distribution function, where D_m is the mean particle size, and σ corresponds to the standard deviation of the distribution. For cross-sectional analysis of the nanoparticles after pressure sintering, the pellets were cut and mounted on the SEM holder using carbon tape. For heat-sintering, the nanoparticles were first deposited on silicon, heated at 150 °C for 20 min, and then transferred to the SEM holder, also secured with carbon tape.

Thermogravimetric analyses (TGA), differential scanning calorimetry (DSC), and Fourier-transformed infrared spectroscopy (FTIR)—Thermogravimetric analysis was conducted to assess the organic content of the NPs. The weight variations were measured from 10 to 800 °C in an air/argon atmosphere, with a heating rate of 10 °C min⁻¹, using a Q600 TA Instruments STD/DSC/TG system. Differential scanning calorimetry analysis was performed to assess the structural

integrity of the lignin before and after the synthesis of the CuNPs, using a Q2000 differential calorimeter from TA Instruments. A mass (~10 mg) of the samples was placed in a hermetically sealed DSC pan. The samples were heated from 0 to 200 °C at a rate of 10 °C min⁻¹ over two heating/cooling cycles under a nitrogen atmosphere. The second heating ramp was used for result analysis. In addition, Fourier-transformed infrared spectroscopy in the range of 200–3000 cm⁻¹ was used, using a Bruker IFS 66VS. Samples were prepared by mixing and pressing into pellets the powder in KBr at 2% w/w.

Colloidal characterization—The hydrodynamic size of the particles in suspension was measured in ethylene glycol in highly diluted samples (<0.1 mg/mL) using dynamic light scattering (DLS) on a Zetasizer Advance (Malvern), with a solid-state He–Ne laser (λ = 633 nm). However, the colloidal stability of the copper nanoparticles with time was measured in a formulated ink containing 90% Methoxydipropylol(1-methoxy-2-propanol), 10% Dipropylene glycol (w/w) and 5% NPs (50 mg_{NP} mL⁻¹) after being subjected to ultrasonic cavitation for 10 min. Data are provided in Turbiscan® Stability Index (TSI) values obtained during 1 h at room temperature using an optical Turbiscan Lab apparatus made by Formulation Inc.

Four-point probe conductivity measurements—The electrical conductivity of the samples was measured using a 4-point probe system from Ossila Ltd, Sheffield (UK). Conductivity values were estimated using geometric correction factors to account for the sample geometry.^[51] Measurements were performed on samples in pellet form. The particles (in powder) were compressed into disk-shaped pellets using a Perkin–Elmer hydraulic press at 3 tons, maintaining this pressure for 5 min. The resulting pellets had a diameter of 13 mm and a thickness between 0.3 and 0.5 mm (Figure S13, Supporting Information). Conductivity measurements were also performed on strip-shaped samples. Conductive ink strips were prepared by placing a solution of EG containing particles in a line, delimited by scotch tape. The concentration of ink fillers in EG was 20% by weight to ensure proper surface coverage. The strips for electric conductivity measurement had standard dimensions of 8 mm in width, 15 mm in length, and 80 μ m in thickness. After deposition, the strips were left to dry until all the EG had evaporated. Subsequently, the dried strips were heat treated in an oven at various temperatures (100–220 °C) for 20 min.

Acknowledgements

A.S.-O. and Y.F.-A. contributed equally to this work. This work was funded by the European Union's Horizon Europe research and innovation program under Grant Agreement no. 101070302 HyPELignum. M.S. was supported by a Margarita Salas fellowship financed by the European Union-NextGenerationEU and the Plan for Recovery, Transformation and Resilience. We acknowledge the Severo Ochoa Centres of Excellence program through Grant CEX2024-001445-S, the Spanish National Center for Electron Microscopy (CNME ELECMI) at the Complutense University of Madrid, through proposals ELC475-2024 and ELC593-2025, the Electron Microscopy Service at the Centro de Biología Molecular Severo Ochoa (CBMSO, CSIC-UAM) for TEM studies, the Scanning Electron Microscopy Service at the Instituto de Micro y Nanotecnología (IMN-CSIC) and SIDI-UAM for FESEM studies, and technical personnel at the Instituto de Ciencia de Materiales de Madrid (ICMM-CSIC) for ICP-OES, FTIR, DSC and XRD analyses.

Funding

European Union's Horizon Europe. Grant Agreement no. 101070302 HyPELignum.

Conflict of interest

The authors declare no conflict of interest.

Supporting Information

Supporting Information is available from the Wiley Online Library or from the author.

Keywords

conductive properties, copper nanoparticles, lignins, microwave-assisted synthesis, polyol process

Received: July 30, 2025

Revised: August 22, 2025

Published online: August 26, 2025

- [1] M. B. Gawande, A. Goswami, F. X. Felpin, T. Asefa, X. Huang, R. Silva, X. Zou, R. Zboril, R. S. Varma, *Chem. Rev.* **2016**, 116, 3722.
- [2] Z. Li, S. Chang, S. Khuje, S. Ren, *ACS Nano* **2021**, 15, 6211.
- [3] W. Li, Q. Sun, L. Li, J. Jiu, X. Y. Liu, M. Kanehara, T. Minari, K. Suganuma, *Appl. Mater. Today* **2020**, 18, 100451.
- [4] F. Liu, L. Lorenzelli, *Wearable Electron.* **2024**, 1, 137.
- [5] Q. Huang, Y. Zhu, *Adv. Mater. Technol.* **2019**, 4, 1800546.
- [6] Q. M. Liu, D. B. Zhou, Y. Yamamoto, R. Ichino, M. Okido, *Trans. Non-ferrous Metals Soc. China* **2012**, 22, 117.
- [7] M. K. Ghosh, S. Sahu, I. Gupta, T. K. Ghorai, *RSC Adv.* **2020**, 10, 22027.
- [8] R. Lu, W. Hao, L. Kong, K. Zhao, H. Bai, Z. Liu, *RSC Adv.* **2023**, 13, 14361.
- [9] F. A. M. Alahdal, M. T. A. Qashqoosh, Y. K. Manea, R. K. A. Mohammed, S. Naqvi, *Sustain. Mater. Technol.* **2023**, 35, e00540.
- [10] B. Huaman, J. L. C. K. Sato, S. Kurita, T. Matsumoto, J. Jayadevan, *J. Mater. Chem.* **2011**, 21, 7062.
- [11] K. Takahashi, S. Yokoyama, T. Matsumoto, J. L. Cuya Huaman, H. Kaneko, J. Y. Piquemal, H. Miyamura, J. Balachandran, *New J. Chem.* **2016**, 40, 8632.
- [12] H. Dong, Y. C. Chen, C. Feldmann, *Green Chem.* **2015**, 17, 4107.
- [13] Y. Gao, Y. Liu, D. Zou, *Environ. Chem. Lett.* **2023**, 21, 2399.
- [14] M. Tsuji, *ChemistrySelect.* **2017**, 2, 805.
- [15] B. Corrales-Pérez, C. Díaz-Ufano, M. Salvador, A. Santana-Otero, S. Veintemillas-Verdaguer, V. Beni, M. P. Morales, *Adv. Funct. Mater.* **2024**, 34, 2405326.
- [16] W. Mekseriwattana, N. Silvestri, R. Brescia, E. Tiryaki, J. Barman, F. G. Mohammadzadeh, N. Jarmouni, T. Pellegrino, *Adv. Funct. Mater.* **2024**, 35, 2413514.
- [17] O. Długosz, M. Banach, *Colloids Surf. A Physicochem. Eng. Asp.* **2020**, 606, 125453.
- [18] K. Simeonidis, M. P. Morales, T. Damartzis, N. Maniotis, S. Veintemillas-Verdaguer, *Ind. Eng. Chem. Res.* **2024**, 63, 20651.
- [19] J. Wiklund, A. Karakoç, T. Palko, H. Yigitler, K. Ruttik, R. Jäntti, J. Paltakari, *J. Manuf. Mater. Process.* **2021**, 5, 89.
- [20] Y. Dong, C. Bao, W. S. Kim, *Joule* **2018**, 2, 579.
- [21] F. Fievet, in *Fine Particles*, Vol. 92 (Ed: T. Sugimoto), Marcel Dekker, Inc, New York **2000**.
- [22] K. Yano, T. Ishizaki, H. Sugiyama, *J. Nanosci. Nanotechnol.* **2018**, 18, 5101.
- [23] J. L. Cuya Huaman, I. Urushizaki, B. Jayadevan, *J. Nanomater.* **2018**, 2018, 1698357.
- [24] I. Kim, Y. Kim, K. Woo, E. H. Ryu, K. Y. Yon, G. Cao, J. Moon, *RSC Adv.* **2013**, 3, 15169.
- [25] L. Zhu, C. Cui, M. Auersvald, J. Zhang, X. Kuang, X. Xiao, Y. Liao, Z. Zhou, K. M. Van Geem, F. Qi, *ACS Sustain. Chem. Eng.* **2025**, 11, 10001.
- [26] S. Laurichesse, L. Avérous, *Prog. Polym. Sci.* **2014**, 39, 1266.
- [27] B. L. Tardy, E. Lizundia, C. Guizani, M. Hakkarainen, M. H. Sipponen, *Mater. Today* **2023**, 65, 122.
- [28] S. Liu, S. N. Reed, M. J. Higgins, M. S. Titus, R. Kramer-Bottiglio, *Nanoscale* **2019**, 11, 17615.
- [29] M. Beske, S. Cronje, M. U. Schmidt, L. Tapmeyer, *Acta Crystallogr. Sect. B Struct. Sci. Cryst. Eng. Mater.* **2021**, 77, 68.
- [30] K. J. Carroll, J. U. Reveles, M. D. Shultz, S. N. Khanna, E. E. Carpenter, *J. Phys. Chem. C* **2011**, 115, 2656.
- [31] W. D. Yang, C. Y. Liu, Z. Y. Zhang, Y. Liu, S. D. Nie, *RSC Adv.* **2014**, 4, 60144.
- [32] R. J. Sammons, D. P. Harper, N. Labbe, J. J. Bozell, T. Elder, T. G. Rials, *Bioresources* **2013**, 8, 2752.
- [33] P. Vanysek, in *Handbook of Chemistry and Physics* (Ed: D. R. Lide), CRC Press, Boca Raton **2000**.
- [34] J. Djafari, A. Fernández-Lodeiro, D. García-Lojo, J. Fernández-Lodeiro, B. Rodríguez-González, I. Pastoriza-Santos, J. Pérez-Juste, J. L. Capelo, C. Lodeiro, *ACS Sustain. Chem. Eng.* **2019**, 7, 8295.
- [35] K. Chung, J. Bang, A. Thacharon, H. Y. Song, S. H. Kang, W. S. Jang, N. Dhull, D. Thapa, C. M. Ajmal, B. Song, S. G. Lee, Z. Wang, A. Jettybayeva, S. Hong, K. H. Lee, E. J. Cho, S. Baik, S. H. Oh, Y. M. Kim, Y. H. Lee, S. G. Kim, S. W. Kim, *Nat. Nanotechnol.* **2022**, 17, 285.
- [36] E. Spurio, G. Berton, S. D'Addato, F. Alimonti, P. Luches, *Nanoscale* **2025**, 17, 4132.
- [37] V. J. Keast, *Mater. Charact.* **2012**, DOI: [10.1016/j.matchar.2012.07.013](https://doi.org/10.1016/j.matchar.2012.07.013).
- [38] C. Kim, G. Lee, C. Rhee, M. Lee, *Nanoscale* **2015**, 7, 6627.
- [39] J. Peng, B. Chen, Z. Wang, J. Guo, B. Wu, S. Hao, Q. Zhang, L. Gu, Q. Zhou, Z. Liu, S. Hong, S. You, A. Fu, Z. Shi, H. Xie, D. Cao, C. J. Lin, G. Fu, L. S. Zheng, Y. Jiang, N. Zheng, *Nature* **2020**, 586, 390.
- [40] B. Zhang, A. Damian, J. Zijl, H. van Zeijl, Y. Zhang, J. Fan, G. Zhang, *J. Mater. Sci. Mater. Electron.* **2021**, 32, 4544.
- [41] J. Zaanen, *NPJ Quantum Mater.* **2023**, 8, 26.
- [42] G. Dyos, in *The Handbook of Electrical Resistivity: New Materials and Pressure Effects* (Ed: G. Dyos), The Institution of Engineering and Technology, London **2012**.
- [43] A. Pajor-Świerzy, Y. Farraj, A. Kamyshny, S. Magdassi, *Colloids Surf. A Physicochem. Eng. Asp.* **2017**, 522, 320.
- [44] X. Dai, T. Zhang, H. Shi, Y. Zhang, T. Wang, *ACS Omega* **2020**, 5, 13416.
- [45] O. Lame, D. Bellet, M. Di Michiel, D. Bouvard, *Acta Mater.* **2004**, 52, 977.
- [46] D. Tomotoshi, H. Kawasaki, *Nanomaterials* **2020**, 10, 1689.
- [47] T. Valayil Varghese, J. Eixenberger, F. Rajabi-Kouchi, M. Lazouskaya, C. Francis, H. Burgoyne, K. Wada, H. Subbaraman, D. Estrada, *ACS Mater.* **2024**, 4, 65.
- [48] M. L. Ermini, V. Voliani, *ACS Nano* **2021**, 15, 6008.
- [49] T. Cheng, H. Xiao, W. A. Goddard, *J. Am. Chem. Soc.* **2017**, 139, 11642.
- [50] A. T. Smit, M. Hoek, P. A. Bonouvrie, A. van Zomeren, L. A. Riddell, P. C. A. Bruijninx, *ACS Sustain. Chem. Eng.* **2024**, 12, 4731.
- [51] K. Sogut, H. Yanar, A. Havare, S. Yilmaz, *J. Semicond.* **2015**, 36, 82001.